Momentum Analysis of Cosmogenic Muons in the MINOS Detectors

A thesis submitted in partial fulfillment of the requirement
for the degree of Bachelor of Science with Honors in
Physics from the College of William and Mary in Virginia,

by

Daniel Damiani

Accepted for _____
(Honors)

_____
Advisor: Prof. Jeffery Nelson

_____
Prof. John Delos

_____
Prof. Jan Chaloupka

_____
Prof. Nahum Zobin

Williamsburg, Virginia
May 2006

Abstract

Proper reconstruction of muon tracks requires that the magnetic fields in the two MINOS detectors be well understood. Previous work revealed problems with the measured ratio of reconstructed cosmic ray $\mu+$ to $\mu-$ in certain regions of the detector indicating that the current model of the field for those sections was unsatisfactory. Modeling of the effects of the ends of both detectors and the supermodule gap of the far detector had been left out of the model of the magnetic field because the old finite analysis based method was too memory intensive and slow to use in track reconstruction. A new implementation of the end and supermodule gap effects was created using a piecewise linear fit to the old end effect model to better model the field in the problem regions. The magnetic properties of the detector steel were also characterized to correct additional problems with the detector magnetic field. Cosmic ray muon data for the near detector was also analyzed. The charge sign ratio of the muons analyzed was 1.27 ± 0.074 which was in line with previous results.

Acknowledgments

I would first like to thank my advisor Professor Jeff Nelson for making this research possible through his guidance, support and always helpful feedback. I would also like to thank Dr. Francisco Yumiceva for his invaluable assistance with my code development and ever present willingness to help. Lastly I wish to thank the Honors Committee for the time they have spent evaluating my research.

Contents

List of Figures

List of Tables

1 Introduction

The charge sign ratio in cosmic ray muons is useful in estimation of the average charge as a function of energy per nucleon of the nuclei of primary incident cosmic rays [1]. Consistent experimental results have yet to be achieved [3]. The most recent data on muon charge ratios comes from the L3 detector at CERN. Muon energy ranges of 20 GeV to 500 GeV were studied near the Earth's surface. Above this energy the muons had insufficient curvature to allow a charge determination. The charge ratio obtained from this data was $1.285 \pm 0.0003 \pm 0.019$ [3]. Figure 1 shows the L3 data, displayed in purple, versus previous experiments.

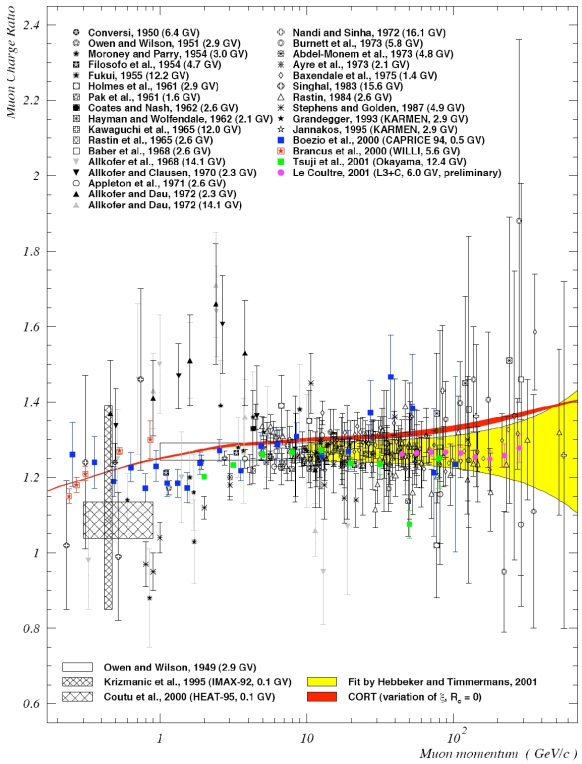

Figure 1: L3 summary plot of world charge sign ratio data as a function muon momentum (GeV/c) [2].

To date, no experiment has made charge sign ratio measurements deep inside the

Earth. As the cosmic ray muons penetrate the rock, they lose energy by ionizing atoms. By going deep underground, one can study muons that originally had significantly higher energies.

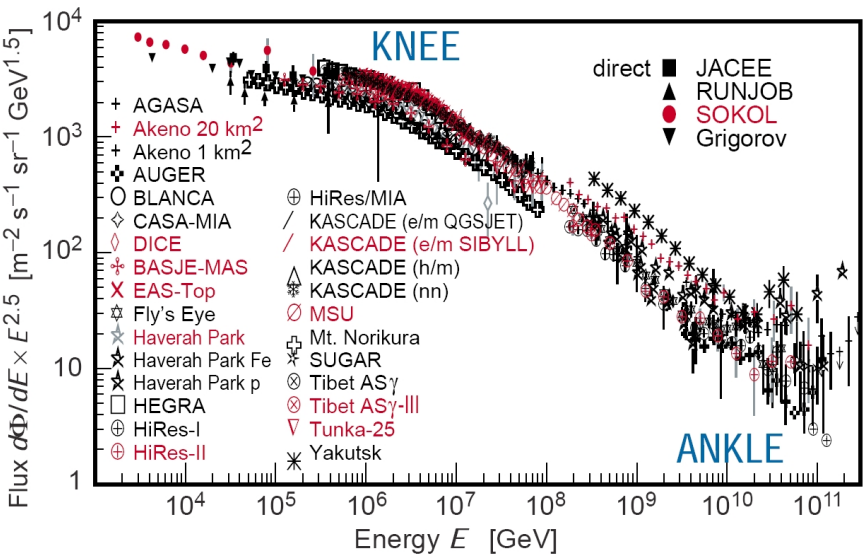

Figure 2: Energy spectrum of primary cosmic rays. The region of "steepening" refers to the area of maximum slope of the data[5].

This project involved the analysis of data from the MINOS detectors in order to study the charge sign ratio of cosmogenic muons as a function of their momentum at moderate depths and deep underground. The data from the MINOS detectors will allow the analysis of a range of muon momenta from 20 GeV to well over 1 TeV. This is the first time data has been collected over this significant of an energy range on a set of detectors based on single detector technology. This range is important because it includes the so called "steepening" or "knee region" (Fig 2) of the primary energy spectrum of cosmic rays [4]. Measurements in this knee region with other techniques vary by as much as a factor of two [5] [6]. Consistent data can be used to constrain and improve the models of cosmic ray showers and cosmic ray sources in this knee

energy range [1].

2 Cosmic Ray Muons

2.1 Basic Properties

The muon, like the electron, tau, and the three flavors of neutrino, is a lepton. A muon has the same charge and spin as a electron, but approximately 207 times the rest mass. Muons are produced primarily by the decay of pions and kaons, $\pi \rightarrow \mu\nu$ and $K \rightarrow \mu\nu$. Muons are unstable and decay into an electron or positron (depending on the charge sign) and two neutrinos with an average lifetime at rest of 2.2 microseconds [5]. Large numbers of muons are produced by primary cosmic rays incident on the upper atmosphere. If the produced muons have high enough momentum, they can, as a result of relativistic time dilation, reach the earth's surface and beyond [7].

2.2 Energy Loss in Matter

In matter muons have a very small cross section for interactions, and as a result they have high penetration power in matter. Muons lose energy in matter by both continuous and discrete methods. The continuous method of energy loss is by ionization of the material through which the muon is passing. The rate of energy loss, dE/dX, is essentially constant for muons moving at relativistic speeds. The magnitude of this energy loss rate is somewhat dependent on the material. The energy loss rate for muons below 1 GeV has a minimum and rises slowly for higher values of energy. For muon energies $E_\mu > 10$ GeV,

$$\frac{dE}{dX} \approx -[1.9 + 0.08ln(E_\mu/\mu)] \tag{1}$$

is a good approximation to better than 5% [8].

In addition to ionization, muons can lose energy through discrete means. This energy is lost by bremsstrahlung, which involves electromagnetic interactions with nuclei of material, as well as direct production of positron-electron pairs. The energy loss by bremsstrahlung is only significant for high energy muons. It manifests itself as discrete bursts of energy along the muons trajectory. The energy loss rate is proportional to E, the energy of the muon, and is given by

$$\frac{dE}{dX} = -\frac{E}{\xi_B(l)} \tag{2}$$

where $\xi_B(l)$ depends on the material. A second although very rare type of discrete energy loss, called a catastrophic loss, occurs when a muon interacts directly with a nucleus [8].

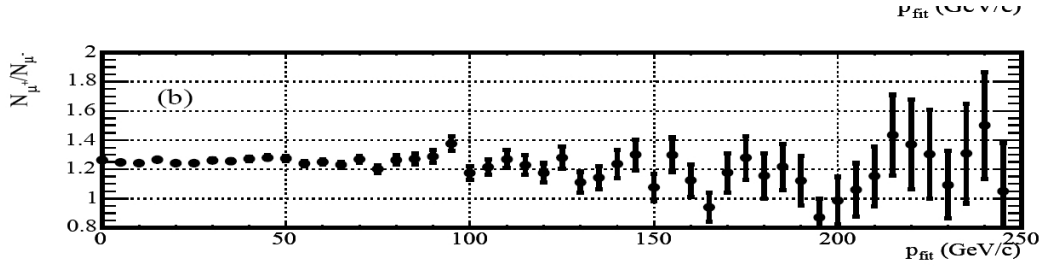

Figure 3: The expected charge sign ratio as a function of muon momentum from Monte Carlo [4].

2.3 Charge Sign Ratio

The antiparticle partner to the muon, μ^-, is μ^+. The charge sign ratio of cosmic ray muons is the ratio of the flux of μ^+ over the flux of μ^- at a specific location. The charge sign ratio, $K_\mu = \frac{\mu^+}{\mu^-}$, can be calculated from the relative abundances of π^- to π^+ and K^- to K^+. The value of the charge sign ratio is dependent upon the average atomic number of the material in which the reactions are occurring. For rock and muons with energies less than 100 GeV where pion decay dominates muon production, $(A \approx 14.5)$ $K_\mu \approx 1.22$. For $E_\mu > 100GeV$ the contribution from kaon decay becomes

significant and the charge sign ratio more difficult to calculate [8]. Figure 3 shows the charge sign ratio for the far detector for Monte Carlo with a truth value of 1.25 [11]. Muons with energies greater than 100 GeV do not curve significantly in the detectors making charge determination more difficult. This is the reason for the deviations from the expected value of 1.25 in the charge sign ratio for muons with energy greater than 100 GeV that is seen in Figure 3.

3 Properties of Ferromagnets

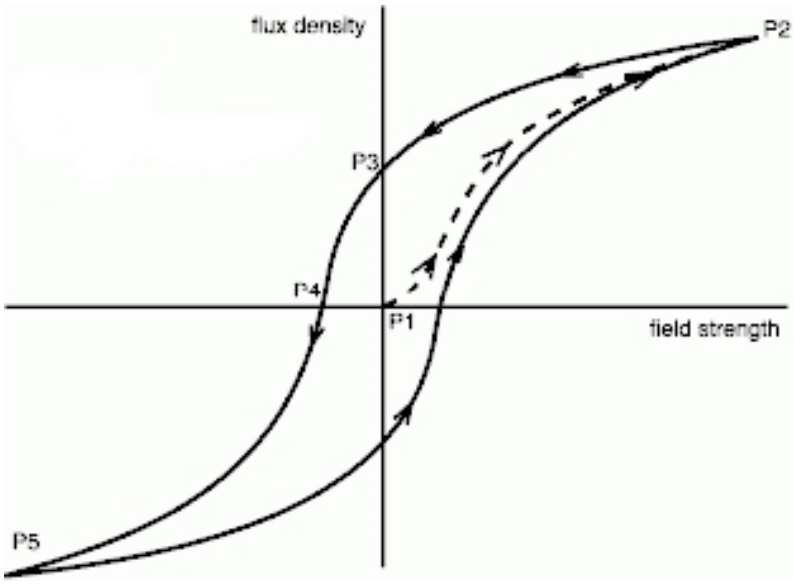

Figure 4: Example of a major hysteresis loop (dotted line is the ramp up) [11].

Ferromagnetic materials will retain a residual polarization even after the polarizing field has been removed. Therefore, the induced magnetic field (B) of a ferromagnet experiences hysteresis as a function of the applied field (H) (called B-H curve) (Fig 4). The point at which the field becomes reversible for higher values of the applied field is called the saturation point. The strength of the B field when the applied field is equal to zero is known as the remanence. In order to return to zero polarization in absence of an applied field a ferromagnetic material must be degaussed. The degaussing

process involves taking the ferromagnet to saturation then to a point slightly less then saturation of the opposite polarity. This is repeated by going to a value of H slightly lesser and opposite polarity than the previous H value (Fig 5) [9].

For constructing the field maps the ramp up curve from zero polarization to saturation under an applied field is most important. An example of this ramp up is portrayed by the dotted line in Figure 4. In order to properly characterize the ramp up of a ferromagnetic material the sample must first be degaussed to remove any polarization.

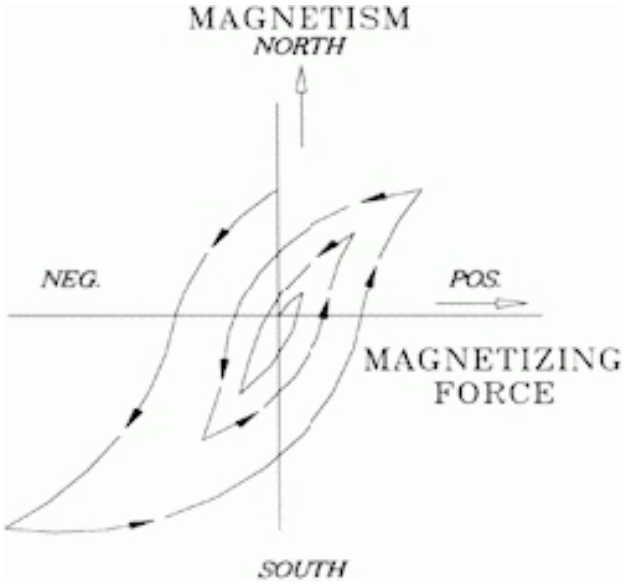

Figure 5: Example of a degaussing[12].

4 Minos Detectors

4.1 Specifications

The data for this project was obtained using the two MINOS detectors. The detectors are part of the MINOS experiment, the goal of which is the observation of neutrino

flavor oscillation. The MINOS detectors are designed to detect muons and therefore indirectly detect muon neutrinos. The near detector is located at Fermilab about 100m below the surface. The far detector is located 714m underground in an iron mine in Soudan, Minnesota.

The detectors consist of planes of steel interspersed with scintillator. The MINOS far detector consists of two equal sized sections of planes separated by a gap, and they are known collectively as the far detector supermodules. Unlike the far detector the near detector consists of a single module. The far detector contains 486 planes of steel and 484 planes of scintillator and weighs 5.4 kilotons, while the smaller near detector contains 282 planes of steel and a lesser number of planes of scintillator and has a weight of about 1 kiloton. Each layer consists of 2.54cm of steel and 1cm of scintillator. High-current coils passing through the detector planes magnetize the steel to an average field of 1.3T in each detector [10].

When ionizing radiation passes through the scintillator, photons are released and pass down optical fibers to photo multiplier tubes (PMTs) that convert the light to an electrical signal and amplify the signal. Using sensitive amplifiers and electronics, the signal is digitized and fed into a data acquisition system consisting of an array of computers. This data is then archived at Fermilab [10]. From this data, the tracks of the muons in the detector can be reconstructed. The energy of the detected muon can be determined by analyzing either the particle's range in the detector or its curvature in the magnetic field. If the muon comes to a stop in the detector its momentum can be determined from its range. If the muon exits the detector its momentum must be determined using the curvature of its track in the detector. In order to accurately reconstruct the momentum of the muon from its curvature the magnetic field in the detector has to be well understood.

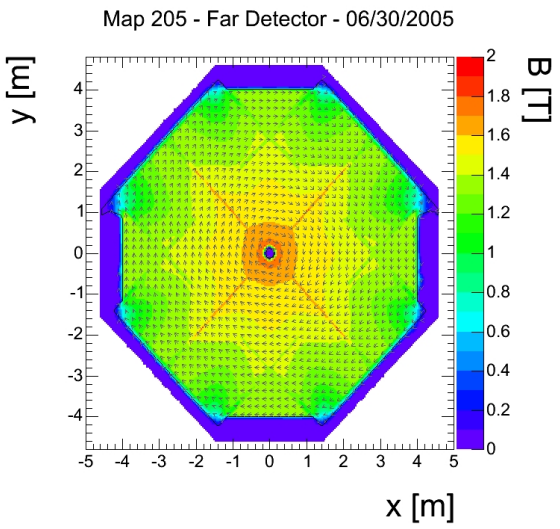

Figure 6: Field map of the single-plane model of the magnetic field for the far detector.

The maps of the magnetic field in the detector were created using a finite element model that utilizes the magnetic properties of steel thought to closely approximate the detector steel. The model used currently to map out the magnetic field is a single-plane model (Figures 6 and 7). The field is computed for hundreds of thousands points distributed in a mesh across a single plane in the detector. Interpolation is used to determine the magnitude and direction of the field for coordinates in the detector that lie between the points of the mesh. The field for this single plane is calculated assuming periodic boundary conditions for a detector with an infinite number of planes. This approximation, while sound deep inside the detector, poses a problem near the detector ends. This problem is discussed in greater detail in the next section.

For the detector ends, similar finite element analysis process was used to generate field maps for the twelve outer planes of each side of the two detectors as well the twelve planes on either side of the gap between the two modules of the far detector.

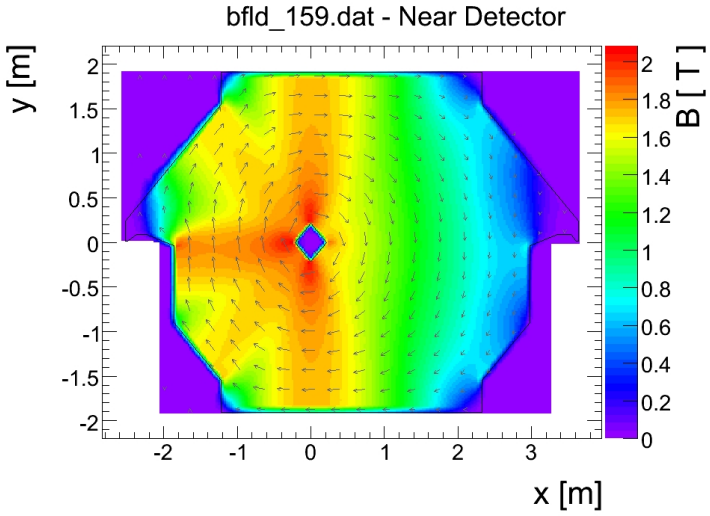

Figure 7: Field map of the single-plane model of the magnetic field for the near detector.

The field map for of each these planes contains over 650,000 coordinate points, and each of these points has seven data values. The sheer size of this of these end-effect models meant that they were never implemented in particle track reconstruction leaving the model of the magnetic fields in the detector incomplete.

4.2 Magnetic Field Problems

Previous work by Brian Rebel, a former graduate student at Indiana University, looking at the charge sign ratio of cosmic ray muons in the MINOS far detector revealed some deficiencies. The charge sign ratio for cosmic ray muons in certain regions of the detectors differed from the Monte Carlo simulations (Fig 8). This demonstrated incomplete modeling of the magnetic fields in those regions.

Deep inside the detector the fields appear to be well understood. The same cannot be said for the ends and outer edges of the detector. The problems with the charge sign ratio revealed regions of the detector where the magnetic field appeared to be less

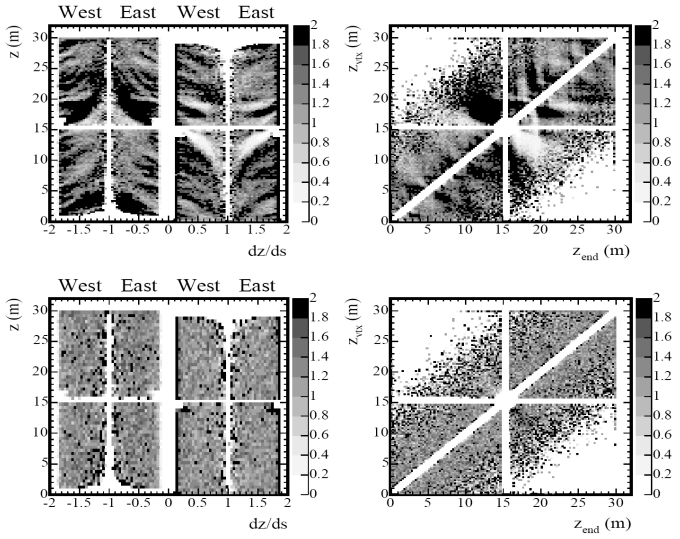

Figure 8: Plot of the charge sign ratio as a function of vertex z-position and dz/ds (indicates the direction of entry into the detector)[4].

well understood than expected. One such region was the ends of both detectors as well as the super-module gap of the far detector. This indicated that the effect of the detector ends on the magnetic field was significant [4]. This significant difference in field meant that the end effects would have to be implemented into track momentum reconstruction in some form. If this was not done, then muon tracks whose trajectory in the detector lay mostly in the one of the ends would have to be discarded because charge and momentum reconstruction of those tracks could not be trusted to be accurate.

Another problem region was at the edges of the detector planes. At the center of the detector planes where the field is strongest the steel of the detector is past the saturation point of its BH curve. Near the edges the field is much weaker and therefore below the saturation point, and hence the characteristics of the BH curve are important in determining the strength of the magnetic field. The problems with

the charge sign ratio in the edges of the detector indicated that the BH curves used in constructing the maps of the magnetic fields in the detector might not accurately reflect the BH curves of the detector steel. In addition the slightly irregular spacing between the detector planes might also be contributing to the problems with the charge sign ratio. This will hopefully be addressed by the use of better alignment surveys.

5 BH Curve Characterization

5.1 Method

Along the outer edges of the two detectors, where the field is lowest, the B-H curve of the steel used in the detector has a greater influence on the magnetic field map. Previously the B-H curve of a steel sample thought to closely approximate those of the actual MINOS steel was used in the calculations of the field maps. As was revealed this appears to have been a poor approximation, meaning the B-H curves of samples of each of the 45 production heats of the steel used in construction of the detectors would have to be characterized.

The MINOS steel samples were machined into tori. These tori were then wrapped with two wire coils, a primary coil of 300 turns and a secondary coil of 200 turns. The completed sample tori were characterized using the W&M version of the Bdot system. The primary component of the W&M Bdot system is a computer controlled power supply, which magnetizes the steel using a primary coil. The ramping field in the steel then induces a current in a secondary coil, which is read back by an analog-to-digital conversion card and then fed back into the PC (Fig 9). A programing language called Labview was used to create the programs to run the Bdot apparatus [13]. In general, these programs will send specified voltage signals read from a text

file to the power supply, which it will then output to the primary coil. The input file also tells the program how long to wait before sending the next signal. The program also controls the sampling of the read back of the induced signal in the secondary coil. The program then integrates the read back signal and sums the areas to construct the hysteresis loops [14].

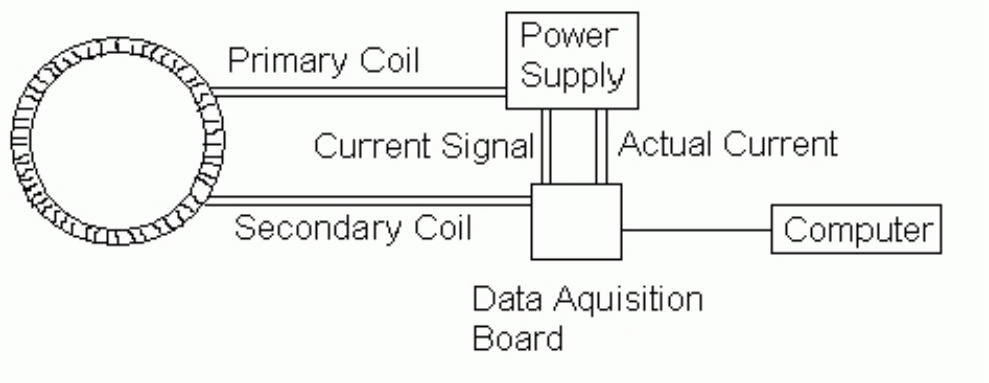

Figure 9: Diagram of the W&M Bdot system [14].

Before data could be taken on the MINOS toruses, the system had to be calibrated and bugs worked out. An input file that properly degaussed the toruses had to be made. Then using three factory made and vendor tested [15] steel toruses the system was calibrated. These toruses were designated 360, 361, and 362 (abbreviations of their heat numbers). During the calibration testing, a roll off in the data was discovered. Above a certain value of the H field the B-H curve's slope would flatten out and fall short of the vendor data. After testing on the apparatus to determine the cause, the problem was that the power supply was having difficulty supplying current over a certain level. It appears that this problem cannot be fixed without replacing the power supply, so no usable data was taken for values of the H field above a certain level.

In the run through of a major hysteresis the programs "Master VT record_v0.6.vi" (36x toruses) or "Master VT record_v0.7.vi" (MINOS toruses) were used. The input degaussing file was "degauss_test_vtvoltshort5.10.txt" and the input file for the main loop was "testfile_longVT_volt5.txt". The torus being tested was degaussed using the program and then run through two major hysteresis loops. The B-H curve data was output to a file, named appropriately, and stored.

A study of the systematics of the system was conducted to see what variations occurred between runs and over longer times. Once the systematics study was completed, testing on the MINOS sample tori began. This was done over the course of one week and data was taken on 26 tori from 21 of the 45 MINOS steel heats. These 26 tori were the ones that had been machined and wrapped by the beginning of the testing period. The machining of the remaining sample tori was completed near the end of the summer of 2005. The tori from the remaining 24 heats were wrapped and tested using the same procedure in early fall 2005.

5.2 Bdot Calibration

The first major goal of the project was to calibrate the W&M Bdot apparatus. In order to accomplish this the apparatus had to degauss the toruses properly after each run. It was discovered that there was a slight offset from zero in the power supply when it was issued a zero volts command. After this offset was corrected, the apparatus could successfully degauss the toruses. The calibration was then able to proceed. The H field was calibrated based on the calculated current in the 36x series toruses, the number of turns in the primary coil, and the physical dimensions of the toruses. Comparing these experimental 36x torus data, with the x-axis data calibrated to units of Amp/m, to the corresponding 36x vendor data, a scale factor for the B field was determined that gave the best fit to the vendor data. After additional

analysis, it was found that multiplying the value of the H field by an additional scale factor of 1.45 allowed for a much better fitting of the experimental data to the vendor data. This scale factor is likely a result of either an inaccurate measurement of the toruses dimensions or a miscalculation in the current flow through the torus. In addition, for all toruses, a roll off was observed for high values of H, this seems to be a result of the current limits of the apparatus's power supply.

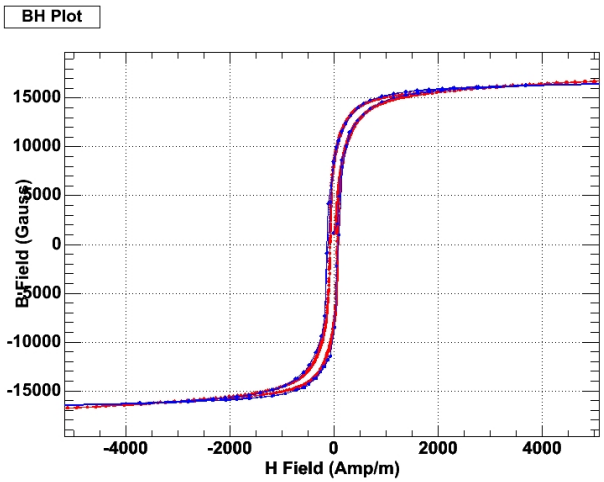

Figure 10: Calibrated 360 torus data (blue) compared with 360 vendor data (red).

The best fitting of the toruses was the 360 (Fig 10) with the 362 being the second best. The 361 torus was somewhat off from the vendor's data with respect to the calibration that worked for the other two toruses. The vendor data for the 361 torus was odd in that it was significantly different from the vendor data for the 360 and 362 toruses, which were both very similar to each other. Since the 361 vendor data contained an unusual offset and required different scale factors for fitting than the other vendor data, it might suggest that there may be something wrong with the 361-vendor measurement. Using the calibration and adjusting for its different dimensions, number of coils and a modest offset, data taken on the 61680 MINOS steel sample torus was calibrated and compared to data for the 362 torus (Fig 11). As can be

seen in Fig 11, the data for the 61680 torus follows the 362 torus data closely until it rolled off which occurred much sooner than for the 36x toruses. This was a result of the lesser number of turns in the 61680's drive coil, meaning to achieve a specific value of H a greater current was needed. Consequently, the roll off occurred for the 61680 as well as the other MINOS toruses for a much lower value of the H field than for the 36x series toruses.

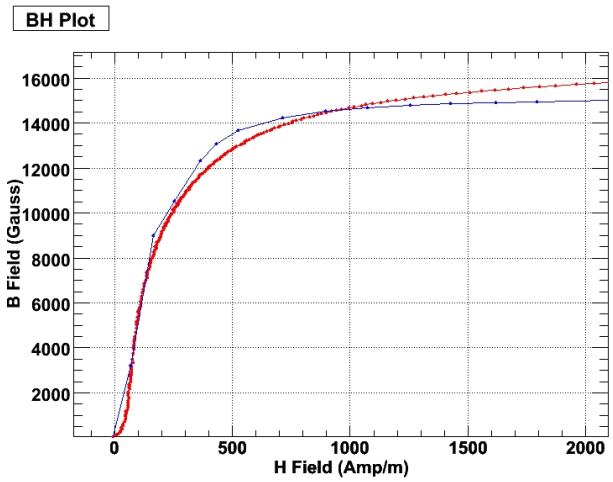

Figure 11: Ramp-up data of 362 (red) and 61680 (blue) toruses.

5.3 Results

Data was collected on MINOS steel sample toruses from all of the 45 heats. These were all machined and wrapped samples. Three data runs were performed on each torus. Once the data collection was completed, the three runs for each torus were averaged to obtain an average plot for each torus. The averaged plots were then plotted to see their spread (Fig 12). These averaged plots were then combined to obtain an average MINOS steel sample plot. Using the data from the averaged toruses a plot of the standard deviation of B as a function of H was made. The standard deviation of B for the MINOS toruses is very comparable to that for the five runs of 362 torus suggesting

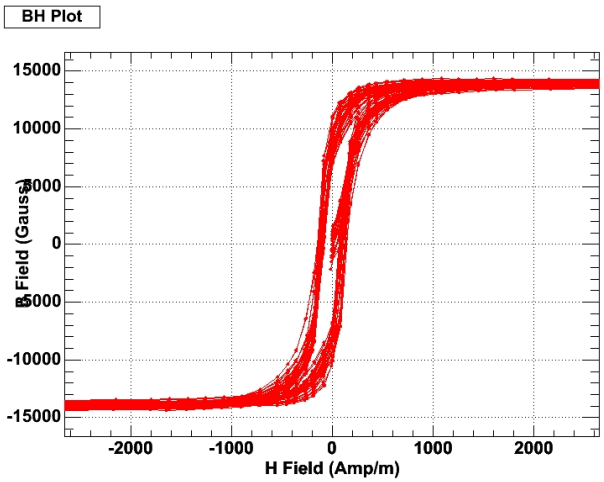

Figure 12: Overlay plot of all 26 tested MINOS steel sample toruses.

that much of the difference between the runs for the different MINOS sample toruses was due to the imprecision of the Bdot apparatus. Figure 13 and 14 show the full B-H curve and ramp up respectively of the averaged MINOS steel sample torus versus the 360 torus vendor data.

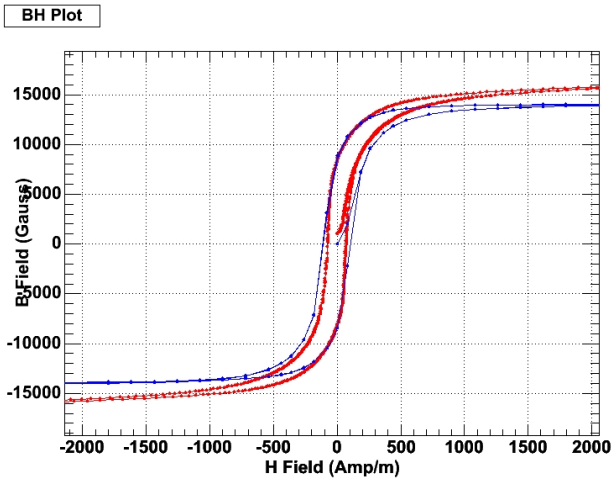

Figure 13: Plot of the averaged MINOS toruses (blue) versus the 360 vendor data (red).

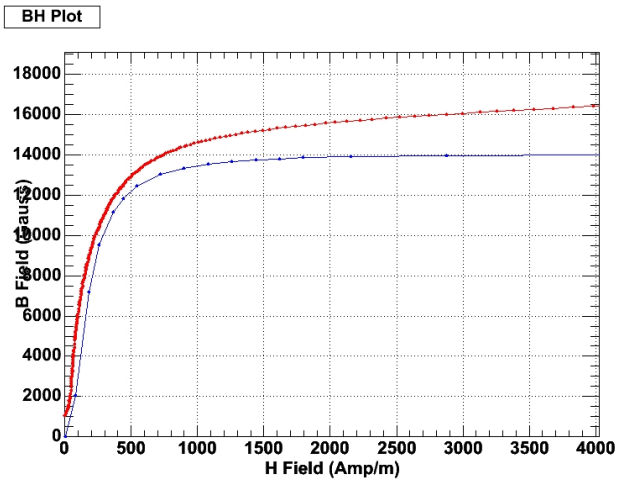

Figure 14: Plot of the ramp up of the MINOS torus average (blue) vs. the 360 vendor data (red).

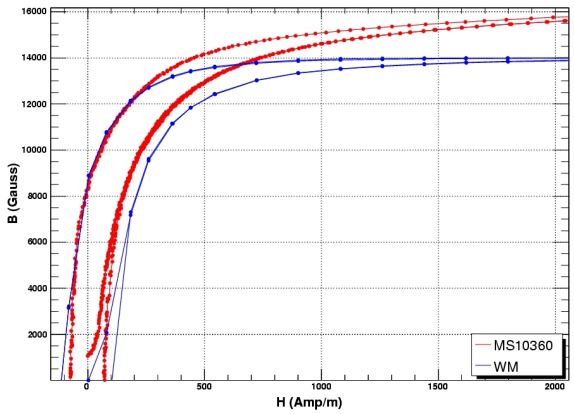

Figure 15: Zoomed plot of the ramp up of the MINOS torus average (blue) vs. the 360 vendor data (red).

6 End Effect Implementation

6.1 Method

As Brian Rebel's research revealed, the magnetic end effects were great enough that they could not be ignored without disregarding data taken there. The previous method for dealing with the end effects was storing values of the field for hundreds of thousands of points in the outer 12 planes of the detector. This involved a substantial amount of data, which was cumbersome and took a large amount of space to store and as a result was never implemented. Developing a simpler method for storing and implementing the end effect data was quite necessary. Ideally such an implementation would also give field values for the ends within 0.5% of the actual magnetic fields.

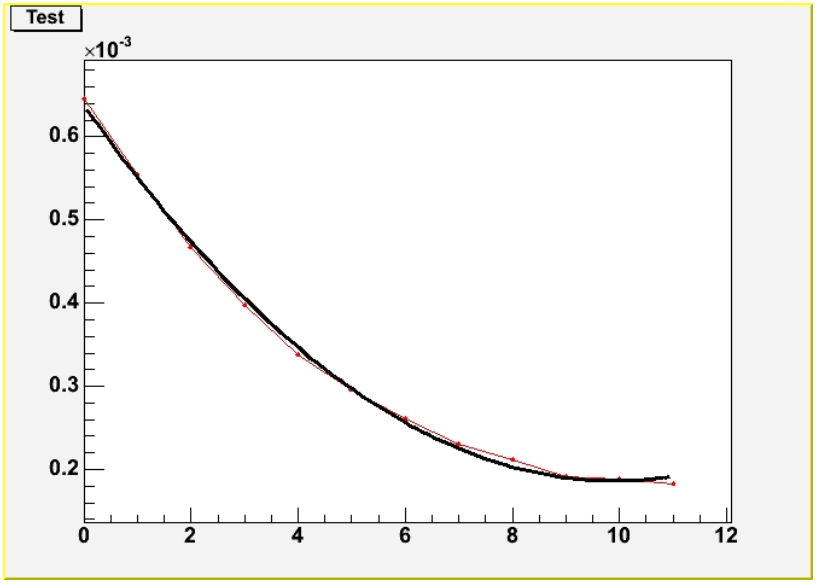

Figure 16: Example fitting to a single detector coordinate. X-axis: plane number, Y-axis: field (Tesla).

The proposed solution to this problem was to fit a function of some type to the data. For a specific point in the detector the corresponding points from each of the

twelve planes would be taken and plotted (on an axis with the planes value on the axis being 0 through 11) and fit with a function (Figure 16). This would allow the data for the twelve points for each coordinate in the detector to be simplified to the parameters for the fit. The main challenges in the process would be finding an appropriate fit type and creating a way to easily implement the fitting.

The program used for the fitting process was implemented using an object oriented data analysis framework called ROOT. ROOT was useful for creating the fitting program because it includes many predefined classes and methods that assist in analyzing and graphing of data. Using ROOT involves writing scripts in C++ which are compiled and executed within ROOT. The program was designed to read in the values of the field at each point in the detectors from twelve external files, one for each plane. A specified function was then fit to a specified number of coordinates. For the initial version locations evenly spaced across the detector were selected for fitting. The initial function tested was a second-order polynomial. Also the fits were constrained to the points of the inner most plane. Since the values of the field at the innermost of the 12 planes were very nearly that of the field deep within the detector, the constraints ensured the values from the functions on the innermost plane matched the values for the corresponding points deep in the detector. The code also allowed for comparisons between the fields of the reconstructed planes and the original source data. Although the program was capable of fitting to an arbitrary number of points, a nine-by-nine (half-meter by meter) grid of points from the detector was used for testing so each test could be run in a reasonable time.

6.2 Results from Fitting Implementation

The second-order polynomial fit did a very good job for most of the points tested, but in the vicinity of the return coil and vertical edges of the detector the fits were

not satisfactory. This can be seen in Figure 17 where each graph is a point tested with the magnitude of the field plot as a function of plane. The position of each graph corresponds roughly to the position of its point in the detector. The data was then fit to other functions in order to find a better fit. A flat (constant valued horizontal) function was fit to the data. This was used as a type of control for the purposes of comparison because it corresponded to no end effect correction. The standard deviation of the differences between the flat fit and the end effect data at the outermost plane, about 190 gauss, was significantly greater than that for the second order polynomial fit of about 25 gauss (Table 1 & 2). Linear functions were also fit to the data to see how much this degraded the reconstruction. This was attempted because the linear fit would only require two parameters per point for reconstruction as opposed to three. The reconstruction was degraded by this change with the RMS of differences in field at the outermost plane doubling; however, the linear fit was still quite superior to the flat fit. Inspection of the plots of the magnitude of the field for a point as a function of plane revealed that for the innermost 2-3 planes the slope is essentially zero. Both the linear and polynomial fits were retested excluding the first two and then three planes and constraining the fit to the first included plane. Both the polynomial and linear fits were improved by the exclusions especially in the outer planes. The exclusion of three planes instead of two offered a slight improvement of the RMS of the differences in the outer planes. This improvement was from 46 to 42 gauss for the linear fit and from 19 to 16 gauss for the polynomial fit (Table 1 & 2).

The next fit tested used a piecewise linear function. Based on analysis of the data the code was modified to fit a single linear function from the first plane fit to plane eight constrained at the innermost plane. A second linear function was then fit to the remaining points constrained to the value at the eighth plane (Figure 18). This piecewise linear fit was tested excluding no planes, two planes, or the three innermost

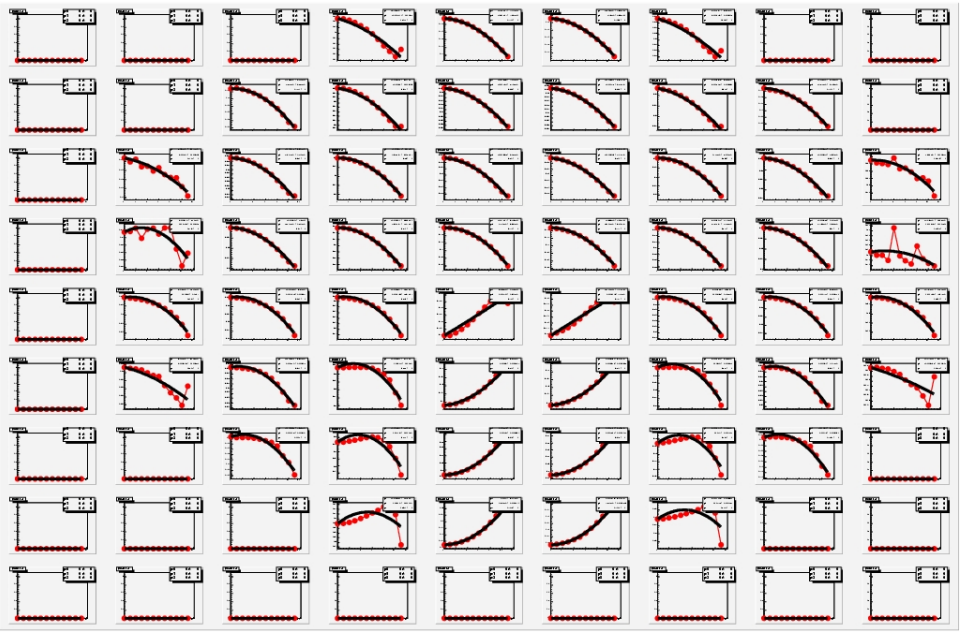

Figure 17: Eighty-one points fit using a 2nd-order polynomial function.

planes. These fits worked quite well and were significantly better at reconstructing the outer planes than both the linear and polynomial fits. At the outermost plane the RMS of the differences was 14 gauss versus 16 and 42 gauss for the polynomial and linear fits respectively. As can be seen in Figure 19 the average differences per plane for the piecewise is significantly smaller than that of both the flat and regular linear fit. The piecewise linear fit was also slightly better than the 2nd order polynomial fit especially in the outer planes. As a result of its better fitting and easier implementation, the piecewise linear fit was chosen to model the end effects for the far detector. The improvements conferred by going from two excluded planes to three were quite small so the decision was made to use the version of the piecewise fit that only excluded two planes.

Now the fits were tested on a greater number of points (5cm by 5cm grid). For the piecewise linear fit excluding the inner two planes the standard deviation at plane zero (outermost) increased from 14 to 23 gauss with 5508 points instead of 81 points.

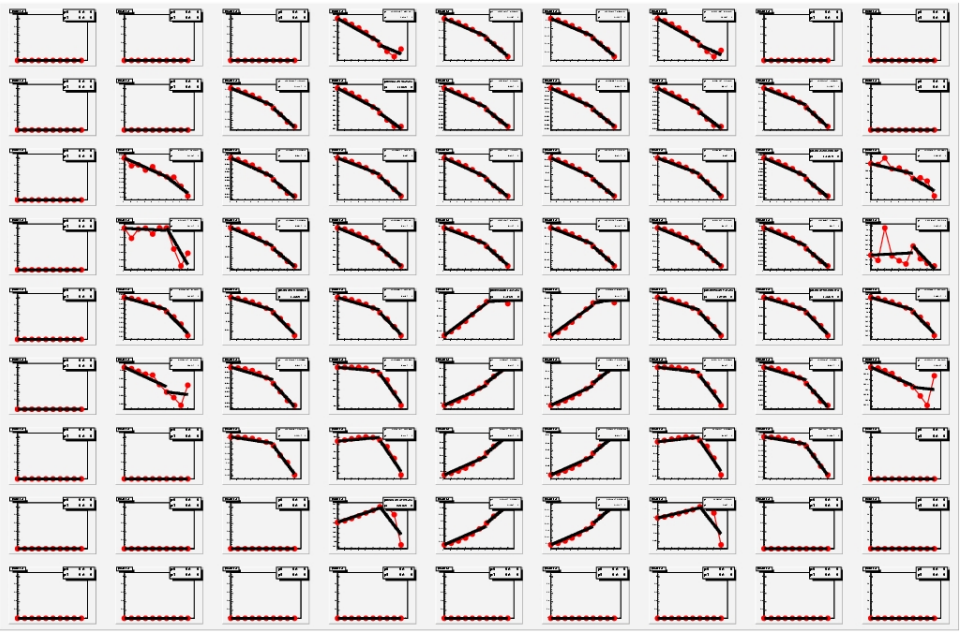

Figure 18: Eighty-one points fit using a piecewise linear fit.

The piecewise fit also maintained its superiority to the second-order polynomial fit for which the RMS at plane zero increased from 16 to 30 gauss. The same piecewise linear fitting method was also applied with similar success to the ends of the near detector. With some changes this fitting method was also applied to the effects of the gap between the two modules of the far detector.

Once the fitting was completed, testing of the data revealed that for both the near and far detectors the single plane model and the innermost of the end effect planes did not match up. A program was written to eliminate the offset, due to different spacings for the finite element analysis, between the single plane model and the end-effect model. For each point the offset was calculated and each point in the twelve planes adjusted to eliminate the offset. This was done for the far detector end and mid module gap as well as both ends of the near detector. The piecewise linear fit was reapplied to each of the adjusted end-effect data sets. An unintended consequence of the offset adjustment was a slight improvement of the fits (Tables 4 and 5).

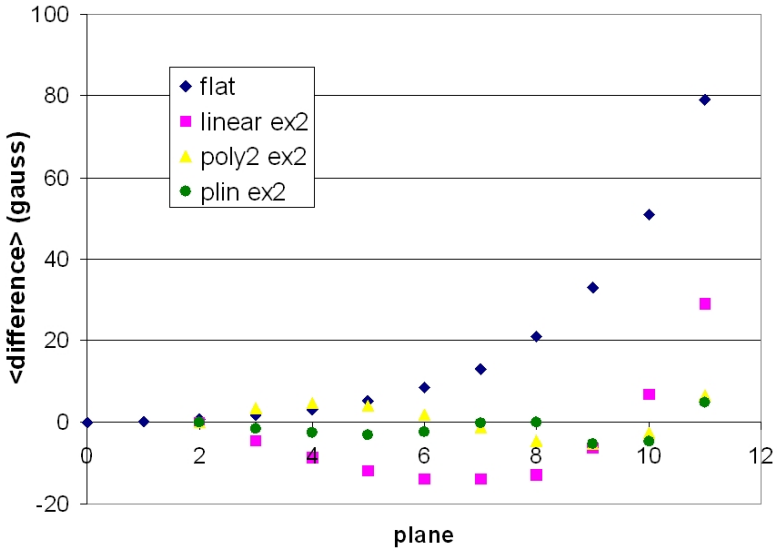

Figure 19: Comparison of the effectiveness of flat, linear, second order polynomial, and piecewise linear fits (the ex2 abbreviation indicates the inner two planes where excluded from the fit).

7 Cosmic Ray Analysis

7.1 Method of Analysis

Cosmic ray muon data in both the MINOS detectors are stored electronically in files. The muon momentum and charge are fitted using standard MINOS software. The results are then stored in ROOT format data structures called trees. The data summary files created by this process are called ntuples, a subclass of the tree data structure in ROOT [16], and contain the events and variables attached to them (such the charge, energy, and start and end point in the detector). The data stored in the ntuples can be used to efficiently analyze the cosmic ray muons.

The first step in the analysis was to use a ROOT based set of tools to extract the needed information from the standard MINOS ntuple files. The smaller files generated from this process were easier to use for analysis proposes. Cuts on the

data could then be added into the code used to analyze the data. These cuts could range from excluding all events whose momentum and charge could not be properly reconstructed to excluding events that pass through a certain area of the detector to requiring that the muons stop within the detector.

7.2 Muon Analysis Results

The analysis was run on the stripped-down versions of 742 ntuple files of near detector cosmic ray data taken during June of 2005. Combined, these files contained 8870 muon events before the analysis cuts were performed. Two cuts were performed on the data. The first removed all events for which the momentum and charge could not be reconstructed accurately because their tracks were either parallel to the field or too straight to make a significant curvature measurement. The second cut was a momentum reconstruction significance cut. Only events for which $|\frac{q/p}{\sigma(q/p)}| > 2.5$ were included in the analysis. The reasoning behind this cut was the lower the value of $|\frac{q/p}{\sigma(q/p)}|$ the higher the chance that the momentum and charge reconstruction were inaccurate. Previous work with the detector showed that this was an appropriate value for the cut [4]. Another cut was one requiring a muon track to pass through a minimum number of detector planes in order to be included. This plane number cut is performed because muons that spend a very short time in the detector were less likely to have their momentum reconstructed accurately. After all cuts were applied the number of events was reduced to 5680 with $N_{\mu+} = 3191$ and $N_{\mu-} = 2489$.

The primary focus of the analysis was the charge sign ratio of the muons as a function of various parameters of the detector. The coordinate system for the MINOS detectors is as follows: the z direction is horizontal in the direction of the beam from Fermilab that passes through the detectors, the y direction is vertical, and the x direction is defined so that it is orthogonal to y and z making a right-handed

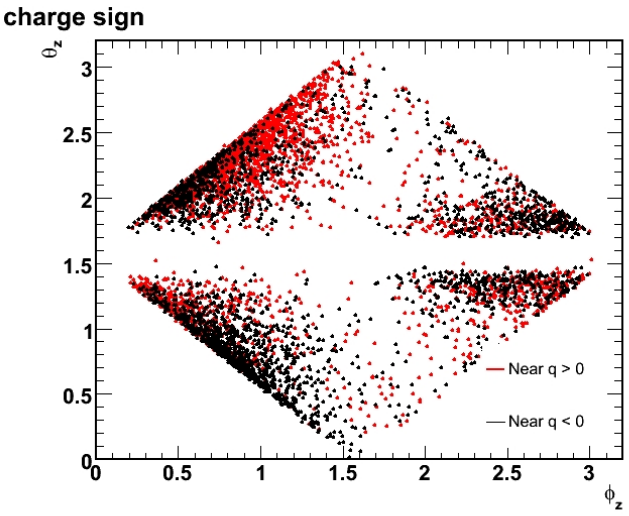

Figure 20: Charge sign in the detector as a function of ϕ_z and θ_z (radians).

coordinate system. Figure 20 shows the charge sign of muon events plotted as a function of the zenith and azimuthal angles in the z direction. The charge distribution observed is the result of focusing of the muon events. At certain points muons of one sign are focused deeper into the detector causing more of that sign to stay in the detector while muons of the opposite sign, are defocused causing more of them to exit the detector. The diagonal lines in the charge distribution from Figure 20 indicate the geometrical acceptance of the detector, which is due to the plane cut and height of the detector.

Figures 21, 22, and 23 depict the number muons of each charge as a function of $cos\theta_z$, azimuth with respect to the z direction (ϕ_z), and energy (GeV). The structure for Figure 22 was close to the expected shape [4]. A greater number of events would have been very useful.

Figures 24 and 25 depict the charge sign ratio of the data as a function of $cos\theta_z$,

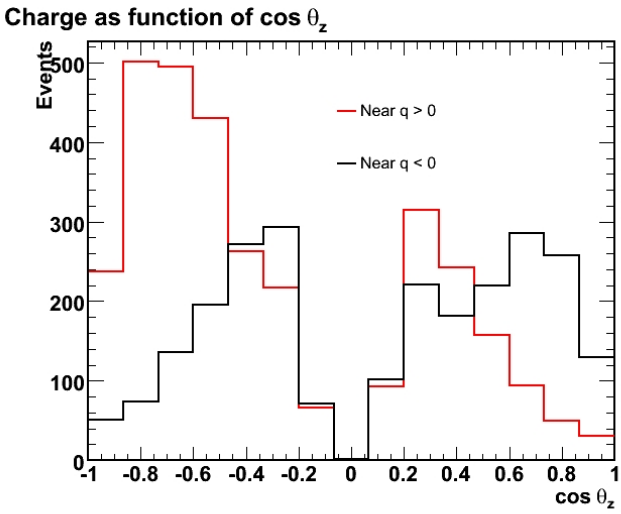

Figure 21: Number of events of each charge as a function of $cos\theta_z$.

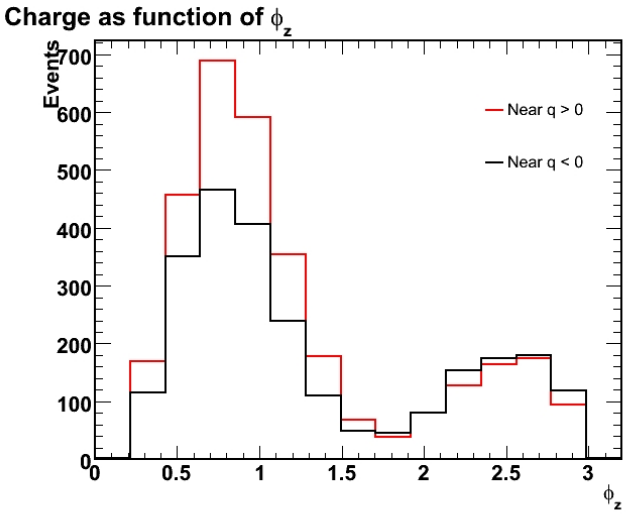

Figure 22: Number of events of each charge as a function of ϕ_z.

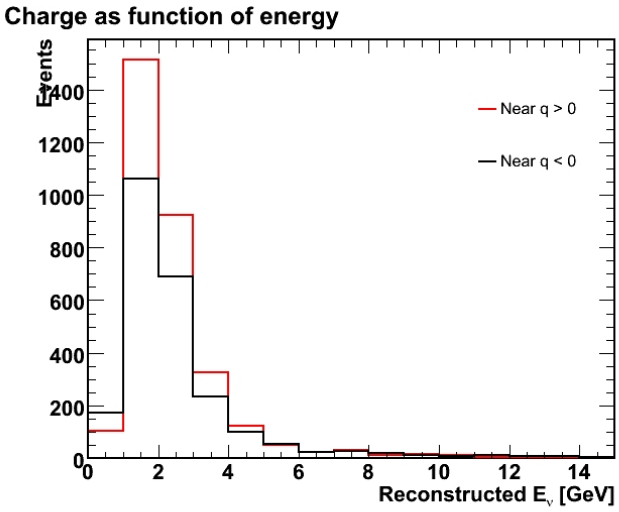

Figure 23: Number of events of each charge as a function of muon energy (GeV).

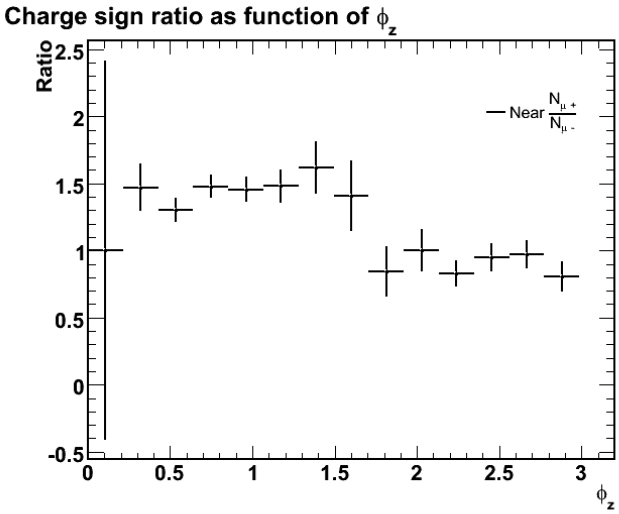

Figure 24: Charge sign ratio as a function of ϕ_z.

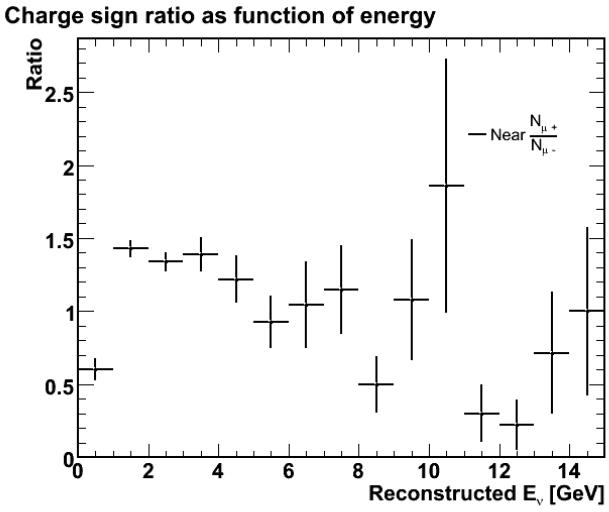

Figure 25: Charge sign ratio as a function of muon energy (GeV).

azimuth (ϕ_z), and energy (GeV). The overall charge sign ratio for the data analyzed was 1.282 ± 0.034. As can be seen from the error and the plots themselves analysis of the charge sign would greatly benefit from an increase in the number of events used.

Figures 26 and 27 show the numbers of muons of each charge and the charge sign respectively as a function of the cosine of θ_y. The parameter θ_y is the angle with respect to the y direction in the MINOS detector coordinates meaning $\theta_y = 0$ points straight up to the surface (zenith), $\theta_y = \frac{\pi}{2}$ points to the horizon, and $\theta_y = \pi$ points down through the earth (nadir). Since the probability of a muon penetrating through the entire planet before reaching the detector is very small, the muons detected for $\cos\ \theta_y < 0$ are muons coming from the surface whose direction was fit improperly by the tracking software. This occurs because the tracking software is optimized for beam events, which are oriented in the +z direction. The problem can be fixed by inverting the track's angle and sign for muon events with $\cos\ \theta_y < 0$.

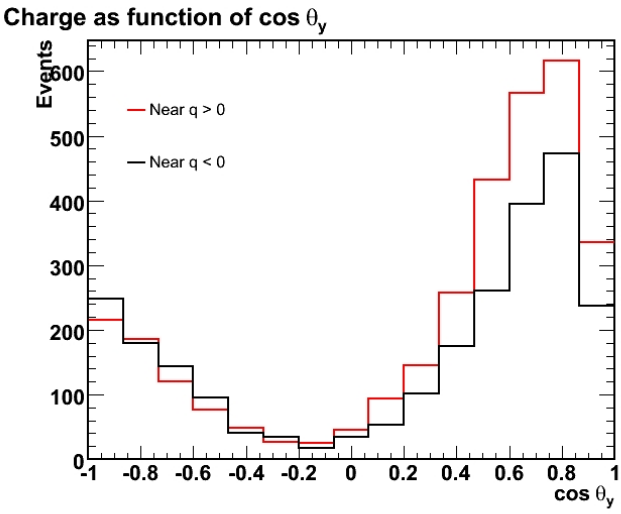

Figure 26: Number of events of each charge as a function of $cos\theta_y$.

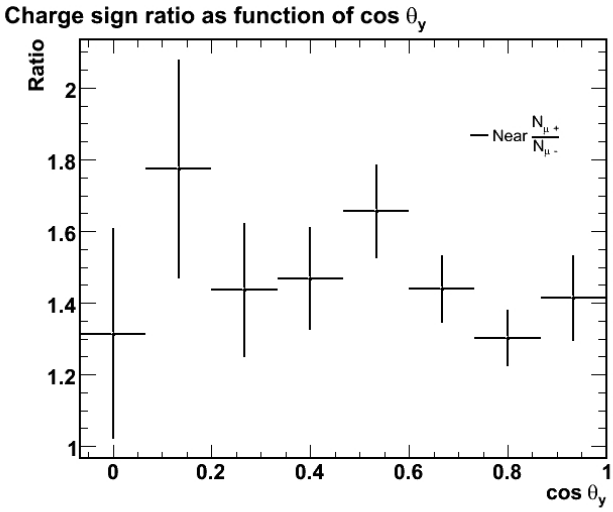

Figure 27: Charge sign ratio as a function of $cos\theta_y$.

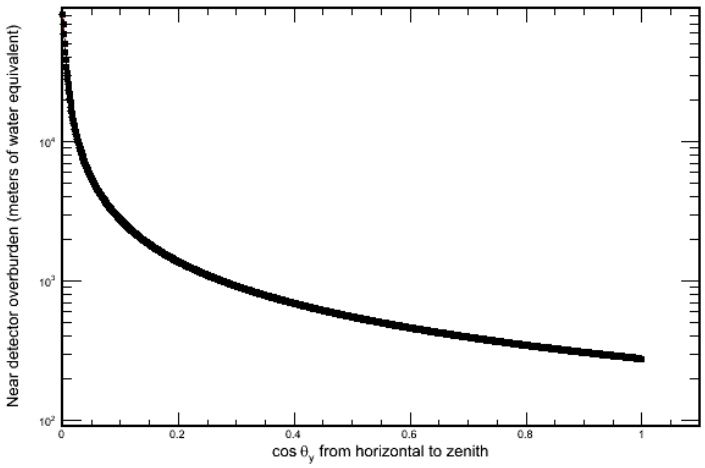

Figure 28: The overburden (mwe) as a function of $cos\theta_y$ for θ from 0 to $\frac{\pi}{2}$.

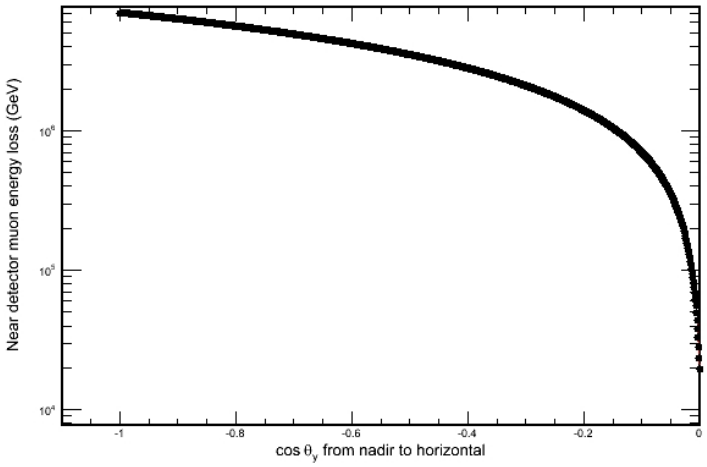

Figure 29: The overburden (mwe) as a function of $cos\theta_y$ for θ from $\frac{\pi}{2}$ to π.

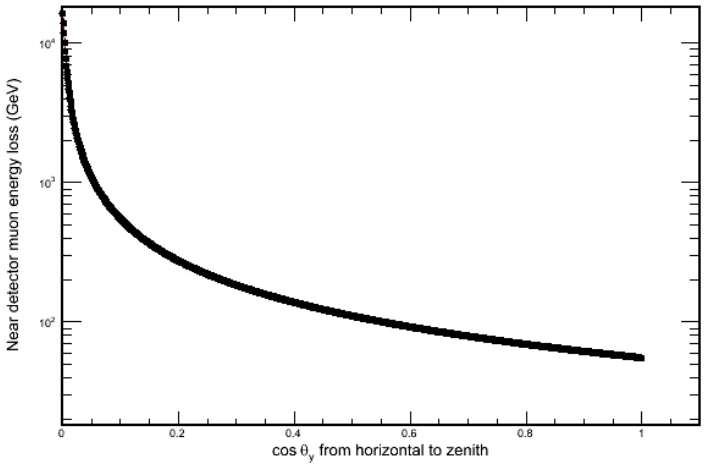

Figure 30: Muon energy loss as a function of $cos\theta_y$ for θ from 0 to $\frac{\pi}{2}$.

The charge sign as a function of this angle is important because the amount of rock, called the overburden, over the detector can be calculated as a function of θ_y. The overburden is given in units of water equivalent (mwe) meaning one meter of rock corresponds to 2.75 meters of water equivalent since the density of the rock above the detector is approximately 2.75 g/cm^3. Figures 28 and 29 shows the overburden as a function of cos θ_y. Since the energy loss of relativistic muons in a medium is nearly constant the energy loss experienced by muons passing through the rock can be fairly easily determined. Using $\frac{dE}{dX} = 2\ MeV/(g\ cm^{-2})$ [8], the energy loss as a function of cos θ_y can be calculated by integration (Figure 30). This means the energy a cosmic ray muon had at the surface can be determined based upon the angle at which it entered the detector. The average value of cos θ_y for the data analyzed was 0.639. This means that the average energy of muons coming from above the horizon was around 90 GeV (average energy loss was 86 GeV and average energy of the muons in the detector was about 4 GeV).

8 Conclusions

Accurate representation of the magnetic field within the MINOS detectors is essential for analysis of muon tracks. With the complete implementation of the detector end effects and MINOS steel BH characterization, the theory-based model of the magnetic field in the detector is complete. It is expected that, this will allow muon tracks to be reliably reconstructed over a larger portion of the detector. This will be tested by the MINOS collaboration this summer.

The preliminary analysis of the cosmic ray muon charge sign in the near detector is complete. These results are consistent with the results from the L3 detector at CERN, which had a charge sign ratio of approximately 1.285 ± 0.0003 compared to the 1.282 ± 0.034 from the preliminary near detector data. The result is somewhat lower than Brain Rebel's result for the far detector of 1.37 ± 0.002 [4]. This difference is expected since Brian's data is for muons of significantly higher energy than those measured in the near detector or L3. It is hoped that updating these results with a significantly larger number of muon events will yield a similar ratio with smaller error.

Future work includes updating the near detector cosmic ray analysis using a significantly greater number of events. Also, an identical analysis will be performed on cosmic ray data from the far detector. Future researchers will take raw cosmic ray data and perform momentum and charge sign reconstruction using a model of the magnetic fields that now includes the end and gap effect implementation as well the MINOS BH curve. This data can then be compared with cosmic ray data not using either of the corrections to see if the regions with problematic charge sign ratios were improved. Also the full scale version of the W&M Bdot system that is on the two detectors will be operational soon and should confirm the detector steel magnetic

calibration.

References

[1] Todor Stanev (Bartol Inst. - coauthor of Ref [5]), Personal communication.

[2] V.A. Naumov, "Atmospheric muons and neutrinos," Proc. of the 2nd Workshop on Methodical Aspects of Underwater/Underice Neutrino Telescopes, Hamburg, August 15-16, 2001 (hep-ph/0201310).

[3] "Measurement of the Atmospheric Muon Spectrum from 20 to 3000 GeV," Physics Letters **B-598**, 15 (2004).

[4] B. Rebel, "Neutrino-Induced Muons in the MINOS Far Detector," Thesis, Indiana University (2004).

[5] PDG, S. Eidelman et al., Physics Letters **B-592**, 1 (2004).

[6] S. M. S. Kasahara, "A study of cosmic ray composition in the knee region using multiple muon events in the Soudan 2 detector," Thesis, University of Minnesota (1997).

[7] M. S. Longair, "High Energy Astrophysics," Cambridge University Press, New York, NY, 1986.

[8] Thomas K. Gaisser, "Cosmic Rays and Particle Physics," Cambridge University Press, New York, NY, 1990.

[9] John R. Reitz, Fredrick J. Milford, and Robert W. Christy, "Foundations of Electromagnetic Theory," Addison-Wesley Publishing Company, Reading, MA, 1980.

[10] "Technical design report for MINOS detectors," The MINOS Collaboration, NUMI-L-703 (1998).

[11] $http://www.ee.surrey.ac.uk/Workshop/advice/coils/BH_hysteresis.png$, July 2005.

[12] $http://www.gaussbusters.com/hysteresis.gif$, July 2005.

[13] Jeffrey Travis, "LabView for Everyone," Prentice Hall PTR, Upper Saddle River, NJ, 2002.

[14] Keith Bechtol, "Measurement of Magnetization Curves of Neutrino Detectors in Conjunction with MINOS," William & Mary, 2004.

[15] KJS Associates Div., Magnetic Instrumentation, Inc., 8431 Castlewood Drive Indianapolis, IN46250.

[16] ROOT Reference Guide, $http://root.cern.ch/root/Reference.html$, April 2006.

A Fitting Data

In all tables "flat" stands for a flat fit, "lin" for a linear fit, "poly" for a 2nd order polynomial fit, and "plin" for piecewise linear fit. The abbreviations "ex2" or "ex3" means that the inner 2 or 3 planes respectively were excluded from the fit.

Table 1: Shows the average difference of the reconstructed fitted field maps and the original FEA maps. Top - innermost plane. Bottom - outermost plane. All numbers in gauss.

	Flat		Lin ex2		Lin ex3		Poly		Poly ex2	
Plane #	< >	RMS	< >	RMS	< >	RMS	< >	RMS	< >	RMS
11	0	0	-	-	-	-	0	0	-	-
10	0.1	2.9	-	-	-	-	3.3	6.4	-	-
9	0.7	7.8	0	0	-	-	5.1	9.8	0	0
8	1.6	16	-4.5	11	0	0	5.4	10	3.4	6.6
7	3.1	27	-8.6	20	-5.0	11	4.4	8.7	4.6	9.3
6	5.3	41	-12	25	-9.3	19	2.2	5.4	4.0	8.8
5	8.5	58	-14	27	-13	23	-0.8	3.4	1.9	5.6
4	13	81	-14	26	-14	24	-4.2	7.7	-1.3	3.1
3	21	107	-13	21	-13	21	-6.9	13	-4.5	8.5
2	33	137	-6.3	15	-7.7	15	-6.5	16	-5.3	14
1	51	167	6.7	20	4.3	16	-1.9	12	-2.6	13
0	79	189	29	46	25	42	9.9	25	6.6	19

Table 2: Shows the average difference and RMS of the differences of the reconstructed fitted field maps and the original FEA maps. Top - innermost plane. Bottom - outermost plane. All numbers in gauss.

	Flat		Poly ex3		Plin		Plin ex2		Plin ex3	
Plane #	< >	RMS	< >	RMS	< >	RMS	< >	RMS	< >	RMS
11	0	0	-	-	0	0	-	-	-	-
10	0.1	2.9	-	-	-1.6	8.1	-	-	-	-
9	0.7	7.8	-	-	-2.8	14	0	0	-	-
8	1.6	16	0	0	-3.6	16	-1.6	6.8	0	0
7	3.1	27	3.2	6.7	-3.8	16	-2.7	11	-1.6	6.1
6	5.3	41	4.1	9.0	-3.4	13	-3.1	11	-2.5	8.7
5	8.5	58	2.9	7.6	-1.9	5.5	-2.4	7.5	-2.4	7.5
4	13	81	0.2	3.7	1.2	7.2	-0.2	1.6	-0.7	1.9
3	21	107	-3.1	5.7	0	0	0	0	0	0
2	33	137	-4.4	12	-5.4	12	-5.4	12	-5.4	12
1	51	167	-2.7	13	-4.7	15	-4.7	15	-4.7	15
0	79	189	5.0	16	4.9	14	4.9	14	4.9	14

Table 3: Near detector - field map version 160 south end.

	Flat		Plin ex2	
Plane #	$< >$	RMS	$< >$	RMS
11	0	0	-	-
10	0.1	2.9	-	-
9	0.7	7.8	0	0
8	1.6	16	3.3	4.7
7	3.1	27	6.2	8.8
6	5.3	41	8.4	12
5	8.5	58	9.2	12
4	13	81	7.2	9.5
3	21	107	0.2	1.0
2	33	137	0	0
1	51	167	19	20
0	79	189	-9.7	10

Table 4: Far detector - field map version 205 - after offset correction.

	Flat		Plin ex2		Plin ex2 post correction	
Plane #	< >	RMS	< >	RMS	< >	RMS
11	0	0	-	-	-	-
10	0.1	2.9	-	-	-	-
9	0.7	7.8	0	0	0	0
8	1.6	16	-1.6	6.8	-1.5	6.8
7	3.1	27	-2.7	11	-2.5	11
6	5.3	41	-3.1	11	-2.8	11
5	8.5	58	-2.4	7.5	-2.2	7.4
4	13	81	-0.2	1.6	-0.2	1.5
3	21	107	0	0	0	0
2	33	137	-5.4	12	-5.0	10
1	51	167	-4.7	15	-4.0	11
0	79	189	4.9	14	4.3	11

Table 5: Near detector south end - field map version 160 - after offset correction

	Flat		Plin ex2		Plin ex2 post correction	
Plane #	< >	RMS	< >	RMS	< >	RMS
11	0	0	-	-	-	-
10	0.1	2.9	-	-	-	-
9	0.7	7.8	0	0	0	0
8	1.6	16	3.3	4.7	2.5	4.0
7	3.1	27	6.2	8.8	4.8	7.4
6	5.3	41	8.4	12	6.5	9.9
5	8.5	58	9.2	12	7.1	11
4	13	81	7.2	9.5	5.6	8.2
3	21	107	0.2	1.0	0.1	0.8
2	33	137	0	0	0	0
1	51	167	19	20	15	17
0	79	189	-9.7	10	-7.5	8.7